J Neurophysiol 110: 1333–1345, 2013.
First published June 26, 2013; doi:10.1152/jn.00957.2012.

Laminar profile of visual response properties in ferret superior colliculus

Iain Stitt, Edgar Galindo-Leon, Florian Pieper, Gerhard Engler, and Andreas K. Engel
Department of Neurophysiology and Pathophysiology, University Medical Center Hamburg-Eppendorf, Hamburg, Germany

Submitted 5 November 2012; accepted in final form 24 June 2013

Stitt I, Galindo-Leon E, Pieper F, Engler G, Engel AK. Laminar profile of visual response properties in ferret superior colliculus. *J Neurophysiol* 110: 1333–1345, 2013. First published June 26, 2013; doi:10.1152/jn.00957.2012.—In the superior colliculus (SC), visual afferent inputs from various sources converge in a highly organized way such that all layers form topographically aligned representations of contralateral external space. Despite this anatomical organization, it remains unclear how the layer-specific termination of different visual input pathways is reflected in the nature of visual response properties and their distribution across layers. To uncover the physiological correlates underlying the laminar organization of the SC, we recorded multiunit and local field potential activity simultaneously from all layers with dual-shank multichannel linear probes. We found that the location of spatial receptive fields was strongly conserved across all visual responsive layers. There was a tendency for receptive field size to increase with depth in the SC, with superficial receptive fields significantly smaller than deep receptive fields. Additionally, superficial layers responded significantly faster than deeper layers to flash stimulation. In some recordings, flash-evoked responses were characterized by the presence of gamma oscillatory activity (40–60 Hz) in multiunit and field potential signals, which was strongest in retinorecipient layers. While SC neurons tended to respond only weakly to full-field drifting gratings, we observed very similar oscillatory responses to the offset of grating stimuli, suggesting gamma oscillations are produced following light offset. Oscillatory spiking activity was highly correlated between horizontally distributed neurons within these layers, with oscillations temporally locked to the stimulus. Together, visual response properties provide physiological evidence reflecting the laminar-specific termination of visual afferent pathways in the SC, most notably characterized by the oscillatory entrainment of superficial neurons.

ferret; oscillations; superior colliculus

THE MAMMALIAN SUPERIOR COLLICULUS (SC) is a highly conserved midbrain structure that responds to novel external events and initiates orienting movements (Stein and Meredith 1993). The SC is organized into several anatomically and functionally defined layers, reflecting its role in sensorimotor transformations. Superficial layers are purely visually sensitive, whereas intermediate and deeper layers receive multisensory inputs and contain premotor neurons that initiate orienting movements (May 2006). Together, all SC layers form topographically aligned visual, auditory, somatosensory and movement field maps of contralateral external space, with the juxtaposition of sensory and motor layers allowing the rapid transformation of sensory signals into orienting motor commands.

The visual system is the predominant sensory modality in the SC, with sensory and motor maps spatially aligned to retinal coordinates (Stein et al. 1999). The sources of afferent pathways innervating superficial and deep layers reflect the functional dichotomy within the SC, with superficial layers being innervated predominantly by retinal and early visual cortical projections, and deeper layers receiving higher visual and motor cortical projections (Harting et al. 1992; Manger et al. 2010; Zhang and Hoffmann 1993). In addition to extensive horizontal connections within individual layers, superficial neurons form axon collaterals that terminate in deep layers, forming a direct superficial-to-deep connection in the SC (Grantyn et al. 1984; Hall and Lee 1993, 1997; Isa et al. 1998). Visual responses in the SC are therefore a product of the interplay between bottom-up inputs from the retina, top-down inputs from the cortex, and intrinsic network dynamics within the SC. Due to the differential anatomical connectivity between different SC layers, this interplay is presumably shifted from retinally dominant inputs in more superficial layers to cortically dominant inputs in deeper layers. We therefore hypothesize that the physiological characteristics of visual responses in the SC vary in a depth-dependent manner, reflecting the laminar organization of bottom-up and top-down visual afferent pathways to the SC. Since both retinal and cortical sources of visual afferent inputs to SC neurons display synchronous oscillatory activity in response to visual stimulation, we speculate that neural response dynamics vary according to the source of visual afferent inputs.

Therefore the goal of the present study was to uncover the key physiological correlates reflecting the laminar organization of visual afferent pathways to the SC in the anesthetized ferret. To achieve this, multiunit activity (MUA) and local field potentials (LFP) were recorded simultaneously from all SC layers with dual-shank multichannel linear probes, allowing for the depth-wise assessment of visual response properties and stimulus driven neuronal correlations. We present here a complete study of basic visual response properties across all SC layers in the anesthetized ferret. Our findings strongly reflect the laminar organization of the SC and the laminar-specific termination profile of retinal and cortical visual afferent pathways. In addition, the layer-specific presence of visually evoked synchronous gamma oscillations in retinorecipient SC layers suggests that oscillatory activity may be driven by bottom-up retinal inputs under anesthesia.

MATERIALS AND METHODS

Seven adult female ferrets (*Mustela putorius*) were used in this study. All protocols were approved by the independent Hamburg state authority for health, environment and animal welfare (BUG-Hamburg). Experiments were performed according to the European Community guidelines for the care and use of animals in scientific experiments (Council of the European Communities Directive 86/609/EEC, 1986), and according to the guidelines of the German Animal Protection Law.

Address for reprint requests and other correspondence: A. K. Engel, Dept. of Neurophysiology and Pathophysiology, Univ. Medical Center Hamburg-Eppendorf, 20246 Hamburg, Germany (e-mail: ak.engel@uke.de).

Surgical Preparation

Animals were initially anesthetized with an intramuscular injection of a combination of ketamine hydrochloride (Gräub, 15 mg/kg), medetomidine hydrochloride (Janssen-Cilag, 0.08 mg/kg) and atropine sulfate (0.15 mg/kg). A tracheotomy was then performed to control the breathing of the animal artificially (Harvard Inspira ASV pump) and supply the anesthesia (isoflurane 0.5–1% in a mixture of 1:1 nitrous oxide and oxygen) for the duration of the experiment. Expired CO_2 was monitored and kept within the range of 3–4% of the end-tidal volume. To prevent dehydration, a cannula was inserted into the femoral vein, delivering a continuous infusion of 0.9% NaCl, 0.5% $NaHCO_2$. Eye movements were prevented by supplying pancuronium bromide (6 $\mu g \cdot kg^{-1} \cdot h^{-1}$) in the infusion solution. Body temperature was maintained at ~38°C with an electric heating blanket, and heart rate was monitored with an ECG. After tracheotomy, animals were placed in a stereotactic frame, and a craniotomy was performed from 1 to 6 mm posterior to the interaural axis, and 4 mm lateral from the midline. The dura was removed to expose the underlying cortex. To prevent exsiccation of cortex, a chamber was built around the craniotomy with dental acrylic, and the cortical surface covered with either NaCl or silicon oil. Phenylephrine (Boehringer-Ingelheim) was applied to the contralateral eye to dilate the pupil and retract the nictating membrane before covering the eye with a contact lens. Finally, the ipsilateral eye was occluded to ensure monocular stimulation.

Histology

To reconstruct the depth of recording positions in the SC, in some experiments probes were coated with DiI (Invitrogen) before insertion. Following completion of electrophysiological experiments, the ferret was perfused transcardially with 4% paraformaldehyde. The brain was carefully removed and postfixed in 4% paraformaldehyde, 30% sugar solution. Coronal sections (50 μm thickness) from the entire SC were prepared with a Leica Jung HN 40 microtome. For sections containing DiI, fluorescent images were captured with a Zeiss Axioskop 40 microscope. These slices were then stained in ammonium silver nitrate solution, revealing the density of myelinated axons (Pistorio et al. 2006).

Stimuli

Visual stimuli consisted of full-field flashes and drifting gratings. Flashes were presented with an LED controlled by a Tektronix AFG 3022 function generator with an interstimulus interval that ranged from 0.66 to 1.66 s between experiments. The LED was projected into an optic cable, which was placed 10 cm from the contralateral eye. From this position, light projected through the optic cable illuminated the entire eye. A total of 500 repetitions were presented per block. Since SC neurons respond well to moving stimuli, random direction small drifting gratings (3°) were used for spatial mapping of receptive fields (RFs). Drifting gratings were presented for 300 ms on a 60 × 60 cm rear-projected screen 57 cm in front of the animal. Stimuli appeared randomly at 400 different positions (20 × 20 stimulation grid) in the ferret's visual field during each stimulus block, which was repeated 10 times for each mapping recording. In addition, full-field drifting gratings were presented for 1 s. To avoid adaptation to certain stimulus features, gratings were presented with various spatial and temporal frequency combinations and eight equally spaced directions (0°, 45°, . . . , 315°). To maintain constant luminance during presentation, drifting gratings were presented on a gray background. Drifting grating stimuli were generated using Psychophysics Toolbox (Brainard 1997).

Data Acquisition and Preprocessing

Recordings were performed using a 2 × 16 dual-shank linear silicon probe with an intercontact distance of 100 μm and intershank distance of 500 μm (Neuronexus, contact size 413 μm^2). Data were acquired with a digital Lynx system (Neuralynx, Tucson, AZ). The probe was lowered into the brain following stereotactic coordinates, while the contralateral eye was stimulated with an LED flash. The surface of the SC was identified by the presence of robust spiking in lower probe contacts in response to flash stimulation. To ensure recording from as many SC layers as possible, probes were advanced so that the uppermost visual responses were ~400 μm below the most superficial recording contact. When a suitable recording position was obtained, the cortex and chamber were covered with low-temperature melting agar (Merck). Data were sampled online at 32.5 kHz, with the raw signal split and band-pass filtered at 1–500 Hz for LFPs and 600–6,000 Hz for MUA, respectively. LFP signals were downsampled to a sample rate of 2.7 kHz. All offline data preprocessing and data analysis were performed using Matlab (Mathworks). After recordings, the LFP signal was further band-pass filtered between 5 and 150 Hz (transition 3.5–5 and 150–151.5, filter order 1,200) both forward and backward to avoid phase shifting. Line noise (50 Hz) and its first harmonic were removed using a notch filter. Finally, the LFP signal was downsampled to 1 kHz. MUA was detected with a positive and negative threshold (Quiroga et al. 2004). To remove artifacts, spikes that were detected on more than three contacts simultaneously were discarded (same sample).

Data Analysis

Current source density. Current source density (CSD) analysis was used to identify physiological markers indicating the relative depth of recording electrodes within the SC to enable the reliable alignment of recording positions across penetrations and animals. CSD profiles were generated using methods previously described by Nicholson and Freeman (1975). The second spatial derivative across the 16 LFP traces on each shank was calculated, resulting in 14 data series representing the direction of net transmembrane current flow at each contact. CSD profiles were calculated on a trial-by-trial basis, and then averaged over all trials. To improve visualization, CSD profiles were interpolated linearly along the spatial axis. Color plots were generated from CSD profiles in which the *x*-axis represents time, *y*-axis depth, and color the net transmembrane current flow at each location. Red corresponds to current sinks, or net inward transmembrane currents, and blue corresponds to current sources, net outward transmembrane currents. The inflection depth (ID), or depth representing the transition between current source and current sink, was readily identifiable across all penetrations using CSD analysis. Therefore, ID was used as a marker to realign all recording penetrations to enable a systematic depthwise analysis of visual response properties across all SC penetrations.

Visual response timing statistics. Peristimulus time histograms (PSTH) were generated by counting spikes in 5-ms bins over all trials, and calculating the average instantaneous firing rate for each time bin up to 600 ms after stimulation. For response latency measures, PSTHs were corrected for prestimulus baseline activity. All bins not exceeding the prestimulus mean firing rate plus two standard deviations were discarded, with only significant time bins remaining ($P < 0.05$). At each visual responsive contact, MUA response latency was defined as the first significant time bin after stimulation.

RF mapping. To quantify RF size and position, we calculated the average spiking response to stimuli presented at each of the 20 × 20 grid positions. A threshold was defined at 50% of the firing rate of the most responsive grid position to separate responsive and unresponsive grid subfields. RFs were defined as the main cluster of all responsive grid subfields. The center of RFs was defined as the centroid of the RF

cluster. Finally, RF diameter was defined as the mean of the width and height of the cluster.

Spectral properties. To estimate the strength of oscillations in discrete spike data, we used the method outlined by Mureşan and coworkers (2008). This method provides a quantitative measure, the oscillation score, which is computed by spectral analysis of autocorrelation histograms (ACH; ±100 ms). Briefly, the oscillation score expresses the ratio between the power of the peak oscillating frequency and the average power of the entire spectrum. To determine the strength of synchronous oscillations between horizontally distributed neurons, cross-correlation histograms (CCH) were computed between ID aligned contacts on each shank in the 500 ms following stimulation. To quantify the strength of oscillations temporally locked to the stimulus, shift predictor (SP) histograms were obtained by computing CCHs with trials on one contact shifted by +1. Fast Fourier transforms were computed on cross-correlation and SP histograms to determine the proportion of synchronous gamma oscillations caused by shared temporal locking to the stimulus. For LFP spectral analysis, spectral estimates were calculated from preprocessed field potentials on a trial-by-trial basis using the FieldTrip Toolbox for MATLAB (Oostenveld et al. 2011). Spectral estimates were obtained for 20 linearly spaced frequencies between 5 and 100 Hz with a 50-ms sliding window incrementing in 5-ms steps. Trials were rejected from analysis if any data points were outside the range of 10 standard deviations of the entire LFP recording. The time-varying raw power was calculated by taking the absolute value of the square of complex spectra. Spectrograms were expressed as a percentage increase in power relative to the prestimulus period (200–25 ms before stimulus onset).

Spike-phase locking. To estimate the spike LFP-phase relationship at different frequencies, spike phase-locking values (PLV) were calculated using spikes recorded from the same contact (Lachaux et al. 1999). The instantaneous phase of the LFP at each frequency was defined as the phase angle between the complex and the real component of the short-time Fourier transform. PLVs were calculated with a sliding window 100 ms in length, and 90 ms overlap (incrementing 10 ms). To avoid potential bias introduced by firing rate modulations, the number of spikes used to calculate PLVs remained constant over time for each recording contact and was defined by the lowest average firing rate from all 100-ms time windows. PLVs were calculated from randomly drawn spikes in each time window 1,000 times to estimate the mean spike PLV for each time point and frequency.

RESULTS

The depth-dependent visual response properties described here were analyzed based on recordings of MUA and LFP activity from 28 SC penetrations (56 probe shanks) in 7 ferrets using dual-shank multichannel silicon probes. From these penetrations, we were able to identify 500 visually responsive MUAs across all depths.

Anatomical Correlates of Flash-evoked Visual Field Responses

To reconstruct probe position in the SC, we used CSD analysis in parallel with histological reconstruction of recording penetrations. In three SC penetrations, we recorded neural activity with fluorescent DiI-coated probes, enabling us to reconstruct the probe trajectory and infer the anatomical location of recording contacts. Figure 1*A* displays an example recording, with DiI fluorescence overlaid onto a myelin stain of the same coronal section. The path of both probe shanks can be seen traversing the various SC layers as fluorescent streaks, with the medial and lateral shanks terminating 1,280 μm and 980 μm, respectively, from the SC surface. The border between the two largest superficial SC layers, the granular stratum griseum superficiale (SGS), and the fiber dense stratum opticum (SO), can be seen as a transition from light to dark staining ~200 μm below the SC surface. Figure 1, *B* and *C*, displays event-related potentials (ERP) and CSD from the medial shank in response to flash stimulation. ERPs at all depths display two components, an early component after ~30 ms, and a late component occurring after ~70 ms. Progressing from superficial to deep recording contacts, both ERP components transform into largely positive deflecting potentials, the amplitude of which is attenuated in the deepest layers. ERPs across all recording penetrations displayed a similar depth profile, characterized by the emergence of large positive deflecting potentials at a certain depth. CSD analysis was used to visualize depth-related changes in LFP responses to flash stimulation. CSD profiles in all SC penetrations were characterized by the presence of a current source immediately above a current sink. The transition between current source and sink, or ID, represents the location with no net current flow. In this example, the ID corresponds approximately to the border between the SGS and SO. Interestingly, later ERP components display a similar source/sink organization, reflecting the depth of ERP polarity reversal, with the late component ID being located ~100 μm deeper. The anatomically inferred location of the ID in this example was typical for all cases in which DiI was used to reconstruct probe position. Since CSD profiles

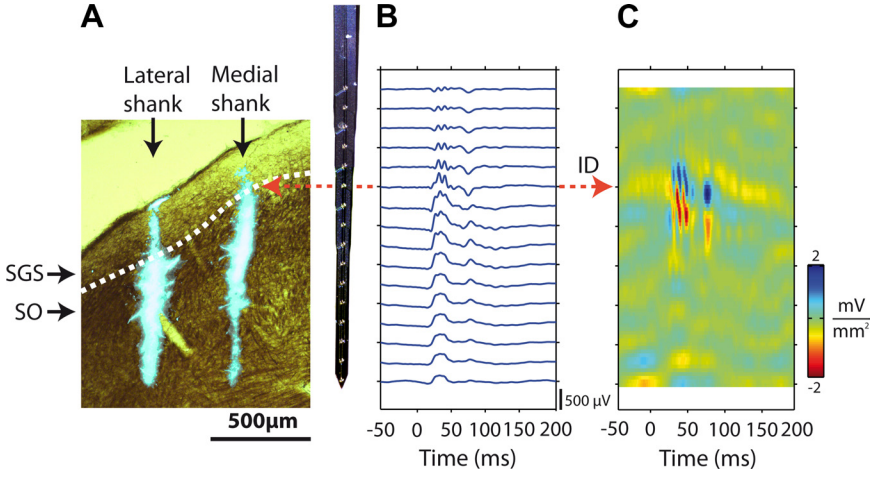

Fig. 1. Inferring probe position through current source density (CSD) analysis. In some recordings, probes were coated with DiI before insertion to enable reconstruction of the recording position using fluorescence microscopy. *A*: example penetration with DiI fluorescence overlaid onto a myelin stain of the same section. The path of both medial and lateral shanks can be seen as two fluorescent tracts terminating at 1,280 μm and 980 μm below the superior colliculus (SC) surface, respectively. A dotted white line represents the border between the two main superficial layers. To the *right* of the section is a scaled image of a recording probe positioned to the same depth as the lowest fluorescence. *B* and *C*: event-related potentials and CSD profiles of the medial shank in *A*, in response to a 2-ms LED flash presented to the contralateral eye. The inflection depth (ID) is visible in the CSD plot as a transition from current source (blue) to current sink (red) and corresponds approximately to the border between the stratum griseum superficiale (SGS) and stratum opticum (SO).

were very similar across all penetrations, we used the ID as a reference to realign all recording positions post hoc, allowing us to perform a systematic analysis of visual response properties across SC layers. Figure 2*A* depicts the population averaged CSD profile following alignment ($n = 51$), with current source and sink above and below the ID, respectively.

Layer-Dependent Spike Responses to Flash and Grating Stimuli

Following alignment of recording penetrations to the ID, we evaluated basic visual response characteristics of SC MUA to flash and drifting grating stimulation. In particular, we focused on average CSD profiles, visual response signal-to noise-ratio (SNR) and response latency of MUA activity. The average CSD profile following flash stimulation (Fig. 2*A*) was more similar to the average CSD following drifting grating offset (Fig. 2*G*) than drifting grating onset (Fig. 2*G*). Spiking SNR was defined as the relative increase in firing relative to the prestimulus period. Figure 2*B* displays the average spike SNR across SC depth for flash stimuli following alignment of penetrations. Similarly, Fig. 2, *E* and *H*, displays the average spike SNR depth profile for the onset and offset of drifting grating stimuli, respectively. The most superficial visual responsive contacts displayed generally short responses to flash stimuli. Contacts from 100 μm above to 200 μm below the ID, representing the presumed lower SGS and SO layers, produced the largest amplitude spiking responses to flashes and tended to maintain a period of high excitability for several hundred

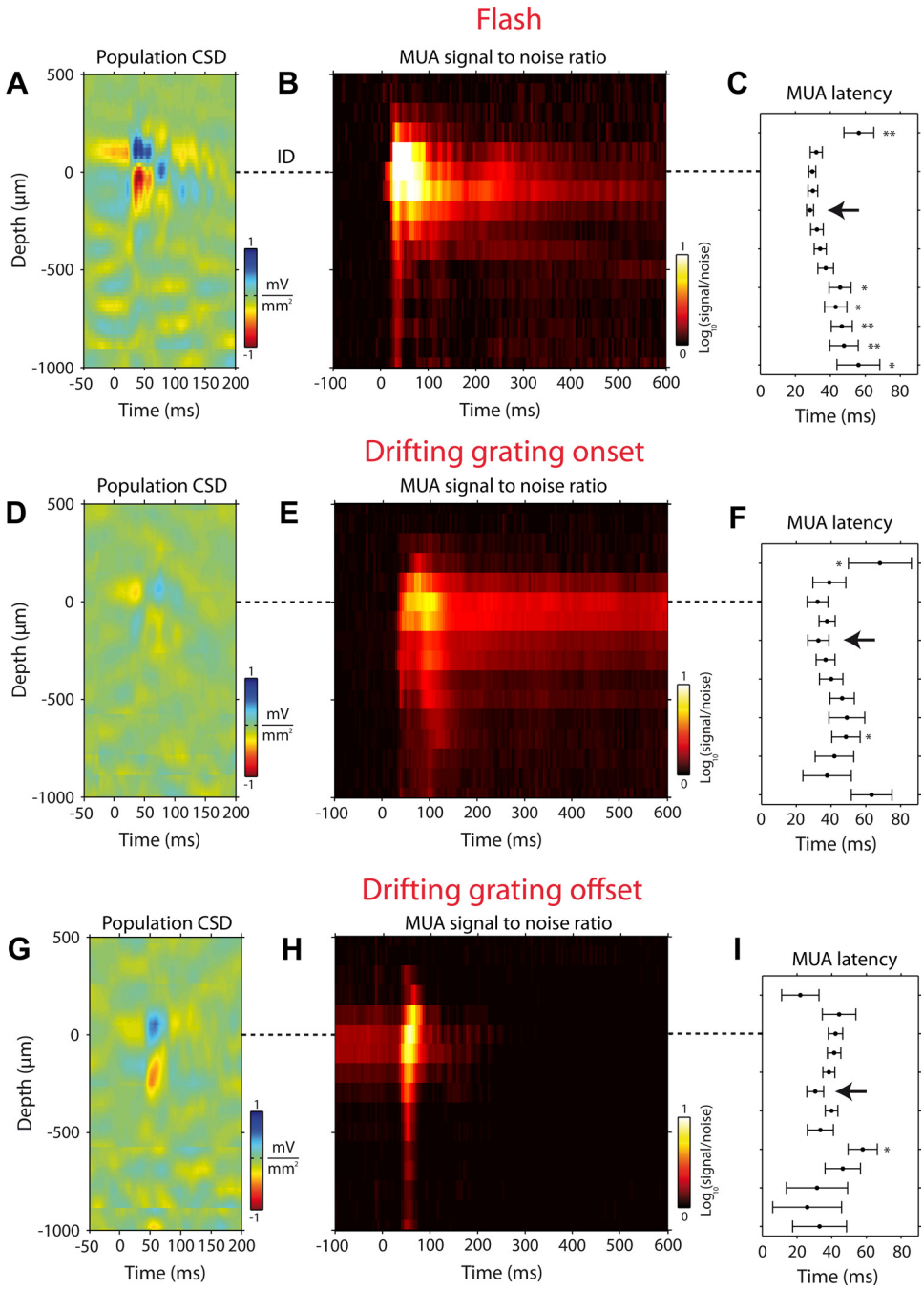

Fig. 2. Average depth aligned responses to flash and drifting grating stimulation for all penetrations. *A*: average CSD profile for flash stimulation following alignment of all recordings to the location of the ID (depth 0 μm). *B*: distribution of multiunit activity (MUA) signal-to-noise ratio (SNR) across depth. Hot colors indicate a larger increase in firing rate relative to the prestimulus period. *C*: population average visual response latency aligned for depth. *D*, *E*, and *F* display the same information as in plots *A*, *B*, and *C*, respectively, but for drifting grating stimulus onset. Similarly, *G*, *H*, and *I* display CSD, spike SNR, and response latency for drifting grating stimulus offset, respectively. Error bars indicate standard error. Significance in each plot was measured with respect to the shortest response (arrow): $*P < 0.01$, $**P < 0.001$.

milliseconds following stimulation. Flash-evoked responses in deeper layers were typically noisier, characterized by a lower amplitude onset response, and in some cases were followed by a period of excitability lasting up to 600 ms poststimulus. Similar to flash-evoked responses, neurons located around the ID displayed the largest amplitude responses to drifting grating stimulus onset and offset. Additionally, neurons in these layers maintained a higher firing rate throughout the sustained period of grating stimulation. Responses in deeper SC layers typically consisted of lower amplitude responses to stimulus onset and offset, with firing rates attenuating to baseline levels throughout the sustained period of stimulation.

Response latencies obtained from flashes and grating stimuli onset exhibited significant depth profiles (ANOVA, $P < 0.0001$), with the earliest responses occurring in the presumed SO region (28 ± 3 ms flash, and 33 ± 6 ms grating, means ± SE), ~200 μm below the ID. Response latencies for flashes, as well as grating stimuli onset and offset, are shown adjacent to spike SNR depth profiles in Fig. 2. For flash stimuli, latencies both above and below the fastest responses were significantly longer. Progressing to deeper layers, response latencies became gradually longer, such that in the deepest visual responsive layers, latencies were significantly longer (56 ± 12 ms flash, ~1,000 μm below ID, $P < 0.01$). Visual responses 200 μm above the ID were generally weak or not present, leading to difficulty quantifying response latency for both flash and grating stimuli (56 ± 8.5 ms, $P < 0.01$ flash; 68 ± 18 ms, $P < 0.05$ grating). The latency of offset responses to grating stimuli did not display a significant depth profile.

MUA RF Properties

In four experiments, MUA spatial RFs were assessed for all visually responsive SC layers. Figure 3*A* depicts spiking RF maps for contacts on both medial and lateral probe shanks for an example recording. On both shanks, neurons respond with higher firing rates to defined stimulus locations in space, visible as hot regions in mapping plots. In this penetration, the most superficial spatial RFs occur 100 μm above the ID (arrows), which is 100 μm deeper on the lateral shank, reflecting the natural mediolateral curvature of the SC layers.

Along each shank, RFs cluster around the same location in the visual field and tend to progressively increase in size with depth, an observation that was consistent across all mapping recordings. To quantify these observations across all penetrations, we calculated the RF centroid and diameter for all visual responsive units. Figure 3*B* displays the location of RF centroids in the ferret's visual field for three representative example recordings (both shanks shown). In each example, RF centroids on each shank cluster around the same location in space. Two penetrations taken from the left hemisphere (red and green) have RFs in the contralateral right visual field. Similarly, recording from the right hemisphere (blue) has RFs in the left visual field. Within each penetration, centroids between shanks appear at a similar horizontal location, with medial RFs appearing higher in visual space than lateral responses, reflecting the topographic organization of the SC. To visualize the variance of RF centroids across all penetrations, we plotted RF centroids with the shank mean as the origin (Fig. 3*C*). The vast majority (85%) of RF centroids lie within 5° of the shank mean, indicating that spatial RFs

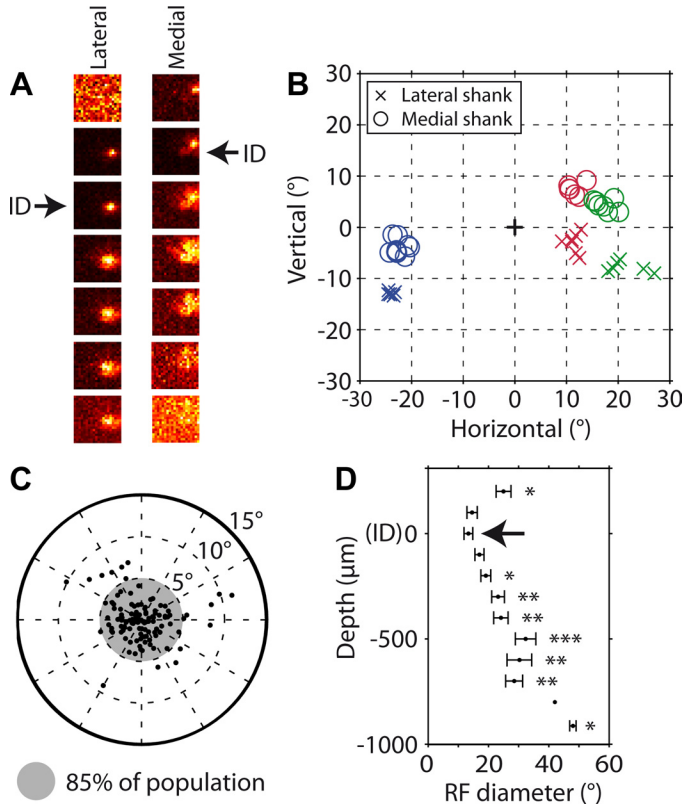

Fig. 3. Spatial receptive field (RF) mapping of SC neurons across depth. *A*: MUA RF maps from both shanks of an example recording. In each plot, hot colors indicate regions in the visual field that respond with higher firing rates. Color axes are scaled for the maximum and minimum firing rate at each contact. Arrows indicate the location of the ID for each shank. *B*: location of RF centroids for 3 example penetrations (different colors) with medial centroids plotted as circles and lateral shanks as x's. The cross indicates the center of the visual field. *C*: all RF centroids plotted with the shank-mean centroid as the origin. Shaded region represents the 85% limit for all centroids. *D*: cross-penetration average spatial RF diameter across depth. Error bars indicate standard error. Significance was measured with respect to the smallest RF diameter (arrow): $*P < 0.05$, $**P < 0.01$, $***P < 0.001$.

maintain topographic alignment across all visual responsive layers.

RF diameters on each shank were aligned to the location of the ID measured from flash stimulation for depthwise analysis across all penetrations. RFs were significantly different across SC layers ($P < 0.0001$, ANOVA). Figure 3*D* depicts the average spatial RF diameter across the depth of the SC. As suggested by the example in Fig. 3*A*, the smallest RFs were located at, and just superior to, the ID (13 ± 1.4° at 0 μm, and 14 ± 1.7° at +100 μm). Progressing from this point through to deeper layers, RF diameters gradually increased such that, at depths 200 μm below the ID, RFs are significantly larger (300 μm: 23 ± 2.1°, $P < 0.01$, 600 μm: 30 ± 4.1°, $P > 0.01$).

Flash-Evoked Gamma Oscillations

We observed a large degree of variability in the profile of spiking responses to flash stimulation, both within individual penetrations and across recording sessions. In general, responses could be characterized into two groups: those displaying periodic temporal structure (oscillatory), and those without periodic temporal structure (nonoscillatory). Figure 4 displays raster plots, PSTHs, and total power spectrograms from pre-

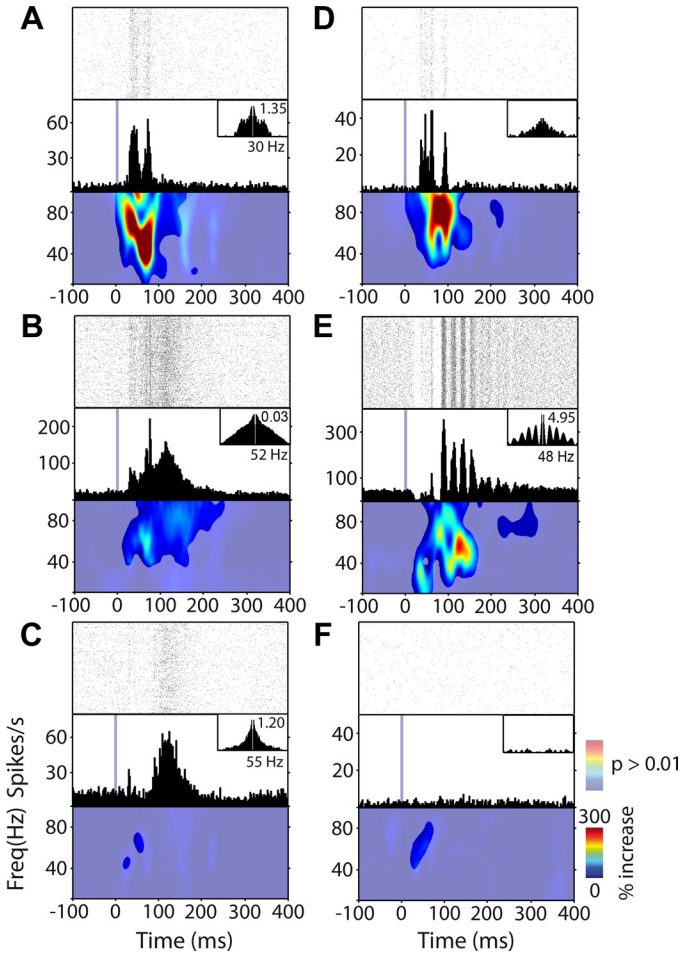

Fig. 4. Diversity of MUA and local field potential (LFP) responses to flash stimulation. *A*, *B*, and *C*: raster plots, peristimulus time histograms (PSTHs), and LFP spectrograms from presumed SGS, SO, and stratum griseum intermediale (SGI) regions along a single SC penetration, respectively. *D*, *E*, and *F*: similar plots to *A*, *B*, and *C*; however, data were taken from a recording performed in another animal. Spectrograms are displayed as a percentage increase in total power relative to the prestimulus period, with a transparency mask representing time/frequency points that were significantly different from baseline activity ($P < 0.01$). Autocorrelation histograms (±100 ms) taken from spikes occurring 0–500 ms after stimulation are plotted as *insets* in the PSTH. For recording contacts that display a sufficiently high oscillation confidence score (>0.7), oscillation scores and frequency are given. The gray line in the PSTH indicates the presentation of the LED flash stimulus (duration 2 ms).

sumed SGS, SO, and stratum griseum intermediale (SGI) regions in two penetrations that exemplify the types of responses observed. The most superficial visual responses were very similar across all penetrations and typically consisted of short, high-frequency bursts of spiking activity, represented as power increases in high-frequency spectral components. In contrast, spiking responses immediately below the ID tended to be larger in amplitude and longer in duration. The most striking difference between the two penetrations shown in Fig. 4 lies in the temporal structure of spiking responses from presumed SO neurons, with Fig. 4*E* displaying strong stimulus-locked oscillatory spiking activity. Flash-evoked oscillatory activity is characterized by the existence of several equally spaced peaks in the PSTH and an increase in gamma power in LFP spectrograms. In contrast, the similarly large magnitude spiking response observed in Fig. 4*C* displays no oscillatory temporal structure, and a comparatively low-power increase in high-frequency spectral components. Oscillatory responses in most cases initiated after ~100 ms, following an initial high-frequency burst of spiking activity. The presence or absence of flash-evoked oscillatory activity in these layers displayed considerable variability between penetrations, both within the same animal and across animals. Deeper contacts tended to respond much weaker to flash stimuli, with small bursts of activity lasting several hundred milliseconds that rarely displayed evidence of stimulus-locked oscillatory patterning. Although the occurrence of flash-evoked oscillatory responses in the SC was variable across penetrations and animals, oscillatory responses were present in at least one penetration in all animals used in this study (summary in Table 1).

To measure oscillatory responses more quantitatively, we computed the oscillation score (Mureşan et al. 2008) for each visual responsive contact. For the examples in Fig. 4, ACHs are plotted as insets in each PSTH. Oscillation scores and peak frequencies are given if the confidence of the oscillations score exceeded 0.7. The example shown in Fig. 4*E* displays a highly structured ACH, with several large-amplitude side peaks, with an oscillation score of 4.95 and a spectral peak at 48 Hz. Responses 200 μm above or below this recording display little or no oscillatory response profile, suggesting that flash-evoked oscillatory firing is a spatially confined phenomenon. For comparison, the example in Fig. 4*B*, also recorded from the presumed SO region, displays an ACH reflective of bursting activity and an oscillation score of 0.03.

Drifting Grating-Evoked Gamma Oscillations

Full-field flash stimuli represent a spatially homogeneous and highly transient stimulus. Therefore, to probe layer-dependent visual response properties for more spatially complex and sustained stimuli, we presented full-field drifting gratings with a variety of spatial and temporal frequency patterns. Figure 5 displays raster plots, PSTHs, and total power LFP spectrograms in response to drifting gratings for the same recording sites as displayed in Fig. 4. In general, spiking and LFP responses were larger for flash stimuli compared with drifting gratings, with responses to gratings typically consisting of bursts of spiking activity following stimulus onset and offset, and comparably low sustained firing rates throughout the presentation of the stimulus. For each example in Fig. 5, ACHs are plotted for sustained and offset responses. Similarly, oscillation scores and peak frequencies are given if the confidence of the oscillations score exceeded 0.7. Perhaps most strikingly, the recording contact that displayed strong stimulus gamma

Table 1. *Incidence of oscillatory penetrations across all animals*

Animal No.	No. of Responsive Probe Shanks	No. of "Oscillating" Probe Shanks
1	8	4
2	5	3
3	6	1
4	7	2
5	8	3
6	6	4
7	12	6

Oscillatory probe shanks were counted if the oscillation score in the gamma frequency range exceeded 2 on any contact.

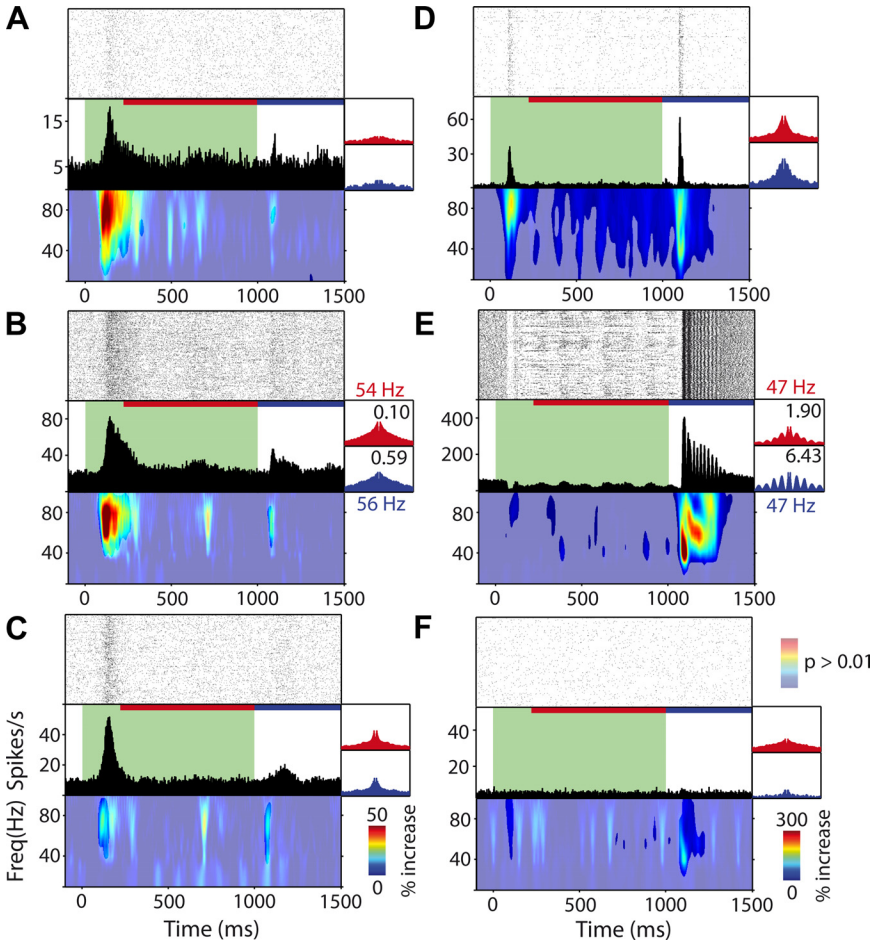

Fig. 5. MUA and LFP responses to drifting grating stimuli. *A*, *B*, and *C*: raster plots, PSTHs, and LFP spectrograms, respectively from the same recording sites displayed in Fig. 3 (*A*, *B*, *C*). *D*, *E*, and *F*: similar plots with data taken from the same penetration as in Fig. 3 (*D*, *E*, *F*). Spectrograms are displayed as a percentage increase in total power relative to the prestimulus period, with a transparency mask representing time/frequency points that were significantly different from baseline activity ($P < 0.01$). Autocorrelation histograms (±100 ms) taken from spikes occurring 200–1,000 ms (red line) are plotted in red, while autocorrelation histograms taken from spikes occurring 1,000–1,500 (blue line) after stimulation are plotted in blue. For recording contacts that display a sufficiently high oscillation confidence score (>0.7), oscillation scores and frequency are given. The green region in the PSTH indicates the duration of the drifting grating stimulus.

oscillatory activity (Fig. 4*E*) to flash stimulation displays very little onset and sustained responses to drifting gratings. Instead, following stimulus offset, neurons engage in very strong oscillatory activity, represented by several poststimulus peaks in the PSTH and a large power increase in the gamma frequency range. In this example, the offset response to grating stimulation displayed a striking resemblance to the highly stimulus-locked gamma oscillatory response observed after flash stimulation. In general, cases that displayed strong flash-evoked gamma activity also tended to display similar activity to the offset of the drifting grating stimulus.

Oscillations Across SC Layers

As suggested by previous examples, we observed the strongest spiking oscillatory activity close to the ID, in the presumed SO region. To confirm this observation quantitatively across all penetrations in all animals, we calculated the percentage of recordings that display certain oscillation scores at each depth for flash (Fig. 6*A*, $n = 52$ probe shanks) and grating stimuli (Fig. 6, *B* and *C*, $n = 27$ probe shanks). For flash stimuli, the greatest number and largest magnitude of gamma oscillatory responses fell into the region directly at, and below,

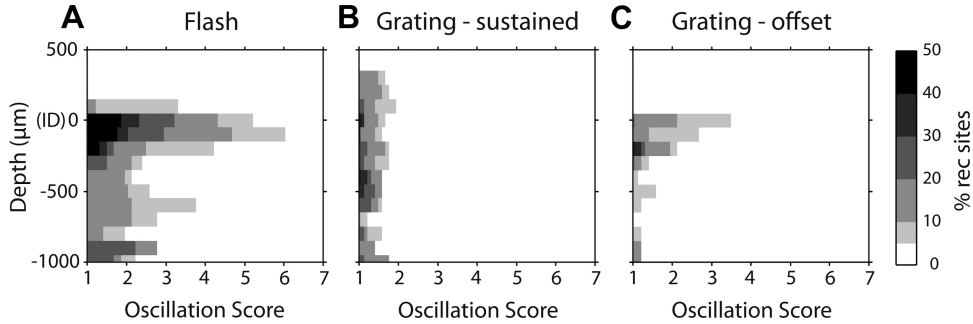

Fig. 6. MUA oscillation score across SC depth. *A*: relative occurrence of gamma oscillations score values following flash stimuli for each recording depth in the SC. *B*: relative occurrence of gamma oscillations score values throughout sustained grating stimuli (200–1,000 ms) stimuli across SC depth. *C*: relative occurrence of gamma oscillations score values following grating stimuli offset (1,000–1,500 ms) stimuli across SC depth. Values are shown in all plots as percentage of recording sites exhibiting oscillations scores and were calculated following alignment of all penetrations in all animals to the ID. Depth 0 μm corresponds to the ID as determined by CSD analysis.

the ID. In this region, 16% of recording contacts displayed an oscillation score above 3, with some cases as high as 9. We observed no significant difference in the peak oscillating frequency across the various layers (data not shown, ANOVA, $P = 0.35$). We observed uniformly weak oscillatory responses across all visual responsive layers during the sustained period of grating stimulation, with no responses exceeding an oscillation score of 2. In contrast, oscillation scores calculated from offset responses displayed depth dependence similar to flash-evoked responses, with strong oscillations detected at and below the level of the ID.

To determine if flash and drifting grating evoked gamma oscillatory activity observed in spiking activity was reflected in the LFP, we measured the occurrence of poststimulus time points that displayed significant power increases ($P < 0.01$) relative to the prestimulus baseline period. Figure 7 displays a depthwise representation of the percentage of recording sites across all animals displaying significant power increases for alpha (8–12 Hz), beta (16–24 Hz), and gamma frequencies (30–60 Hz) for each poststimulus time point. For flash stimuli, a large percentage of recording sites display significant power increases in the first 100 ms following stimulation for all tested frequency bands. These responses in the alpha and beta frequencies reflect the time course of evoked potential produced through such a transient visual stimulus. Although all layers display a high occurrence of significant power increases in the gamma frequency in the first 100 ms, the prolonged response (100–200 ms) is characterized by power increases specifically in layers surrounding the ID. Within these layers, 40% of recording sites displayed significant gamma power increases during the later time period. In contrast, less than 10% of deep layer contacts displayed significant power increases. We observed fewer transient responses in the lower frequency bands for the onset and offset of drifting grating stimuli compared with flash stimuli. As suggested previously by spiking data, we observed a strong occurrence of significant gamma power increases following the offset of grating stimuli that was focused around the ID. Although 36% of recording sites at the ID also displayed a significant gamma power increase in the sustained period of grating stimulation, offset responses were significantly larger than sustained responses in a pairwise comparison (sign test, $P = 0.013$).

Spike Field Coherence

Since the strongest gamma activity in spikes and fields colocalize in the region around the ID, we were interested in the interplay between spikes and fields. To determine the dependence of spike timing on the LFP phase, we calculated the time-resolved PLV following flash stimulation. Spike-phase locking was calculated with a 100-ms sliding window for frequency bands up to 100 Hz. Figure 8 displays the PSTHs and PLV spectrograms for example recordings from the presumed SO region for flash and drifting grating stimuli. Similar to previous examples, PSTHs contain several peaks, indicating a time-locked oscillatory response to flash and grating stimulation. In the corresponding PLV spectrograms, oscillatory

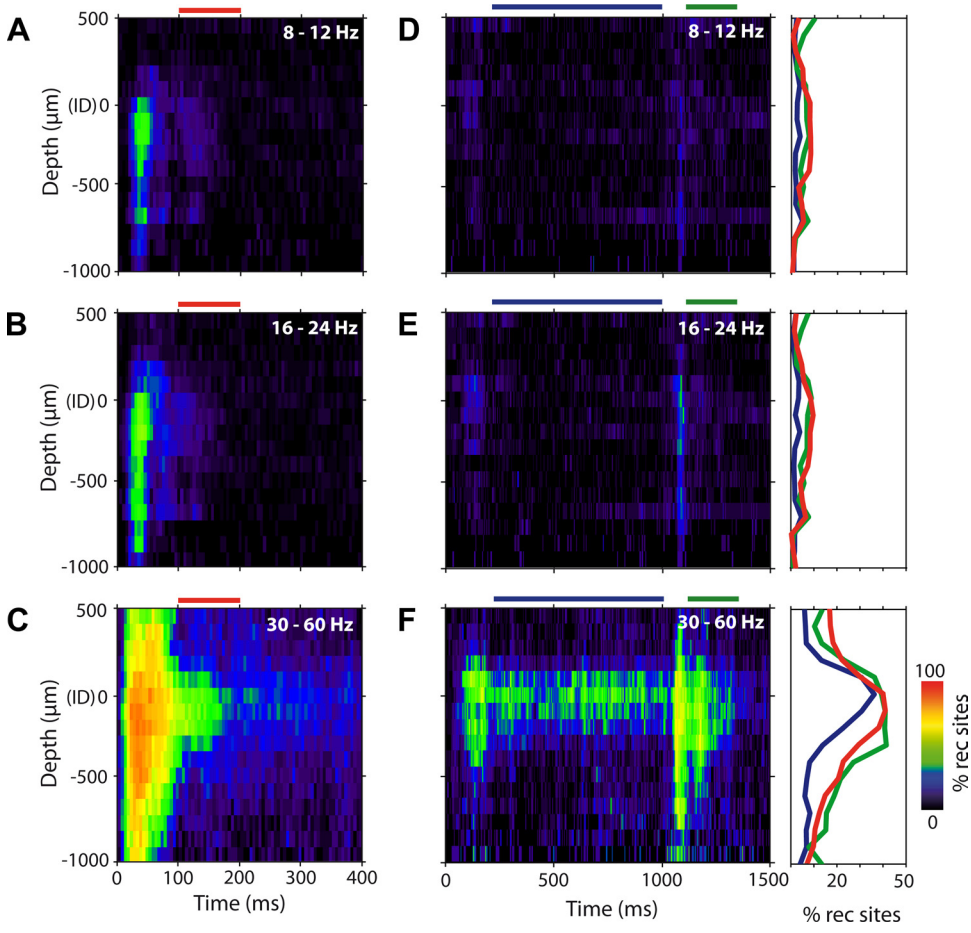

Fig. 7. LFP oscillations across SC layers. *A*, *B*, and *C* illustrate the percentage of recording sites displaying significant power increases in alpha (*A*), beta (*B*), and gamma (*C*) frequency bands across depth following flash stimulation. Likewise, *D*, *E*, and *F* illustrate the percentage of recording sites displaying significant power increases in alpha (*D*), beta (*E*), and gamma (*F*) frequency bands across depth for drifting grating stimuli. Percentages were calculated across all penetrations from all animals following alignment to the ID. To the *right* of *D*, *E*, and *F* are plots representing the percentage of recordings displaying significant power increases during each of the indicated time-windows (flash, 100–200 ms, red; sustained grating, 200–1,000 ms, blue; grating offset, 1,100–1,350 ms, green).

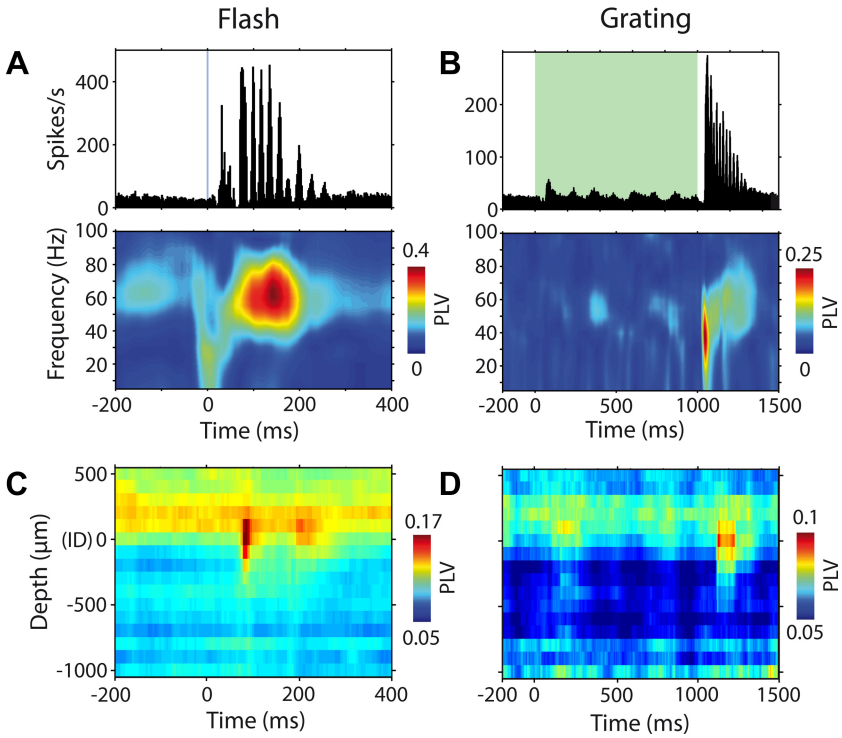

Fig. 8. Spike-phase locking. *A*: PSTH and phase-locking value (PLV) spectrogram for an example flash recording. *B*: PSTH and PLV spectrogram for an example drifting grating recording. Plots *C* and *D* display the average spike PLV across all aligned penetrations in the gamma frequency range for each SC depth for flash and grating stimuli, respectively. The gray line and the green box in *A* and *B* indicate the time of flash and drifting grating stimuli, respectively.

responses are characterized by band-limited increases in spike-phase locking in the gamma frequency range temporally coinciding with oscillatory spiking activity. Therefore, in these cases, spike timing is locked to the phase of fields in the gamma frequency. In general, most recordings displaying flash, and grating-evoked gamma spiking activity also displayed strong spike-phase locking around the oscillating frequency. Figure 8, *C* and *D*, displays the time-resolved average spike PLV in the gamma frequency range for all SC layers for flash and drifting grating stimuli, respectively. In lower superficial and the upper SGI SC layers, flash and grating-offset evoked spiking activity displays strong spike-phase locking at the oscillating frequency of fields, suggesting that neurons are highly entrained to the dynamic fluctuation of local population transmembrane potentials. To determine if oscillating neurons were entrained to local LFP rhythms across all recording contacts, we computed the correlation coefficient between PLVs and oscillation scores. Since we observed the strongest oscillatory responses from 100 μm above, to 300 μm below the ID, we computed correlation coefficients for these layers and all other layers separately (as illustrated in Fig. 9*A*). Correlation coefficients and corresponding *P* values are summarized in Table 2. For flash evoked responses, contacts located around the ID displayed a highly significant correlation between oscillation score and PLV ($R = 0.57$, $P < 0.001$), with other contacts displaying no correlation ($R = -0.07$, $P > 0.5$). These layers displayed a similar significant correlation for the offset to grating stimulation. Interestingly, although other layers did not display strong oscillation scores and PLVs, these values displayed significant correlations for both sustained and offset responses.

Intershank Spike Cross-Correlation

In penetrations displaying gamma oscillatory activity, we often observed oscillations on both shanks at corresponding depths within the SC. To determine how flash and grating evoked gamma oscillations interacted horizontally within SC layers, we investigated the cross-correlation of spiking activity between probe shanks. Cross correlation histograms were computed between contacts at the same relative depth, as determined by the ID on each shank (Fig. 9*B*). To elucidate the nature of coherent oscillations in more detail, we also computed SP histograms, or CCHs, with the trials on one contact shifted by +1. The resultant SP provides an estimate of spike correlation due to co-modulation of firing rates and shared temporal locking to the stimulus. Figure 9*C* displays cross correlation and SP histograms computed between two contacts from the presumed SO region separated laterally by 500 μm. Following flash stimulation, both of these recording sites displayed an increase in spiking activity characterized by prolonged stimulus-locked oscillations. Accordingly, the CCH calculated during the poststimulus period displays a highly modulated structure, with a central peak and several side peaks that decay in amplitude for larger time shifts. Side peaks are separated by between 16 and 25 ms, indicating an oscillating frequency in the gamma range (40–60 Hz). In this example, the SP shares a very similar structure to the raw CCH, indicating correlated spiking activity remains after shifting trials. To obtain a quantitative measure of the relative strength of gamma oscillations between cross-correlation and SP histograms, we computed the power of each histogram in the gamma frequency. Figure 9*D* shows the raw CCH gamma power plotted against SP gamma power for all visual responsive contact pairs. Contacts are separated into two groups according to the relative depth in the SC, as illustrated in Fig. 9, *A* and *B*. Contacts distributed further from the ID had comparatively low gamma power values for both CCH and SP, with no significant correlation present ($R = 0.23$, $P > 0.1$). In contrast, we observed a very strong correlation for contacts close to the ID ($R = 0.98$, $P < 0.0001$), indicating little

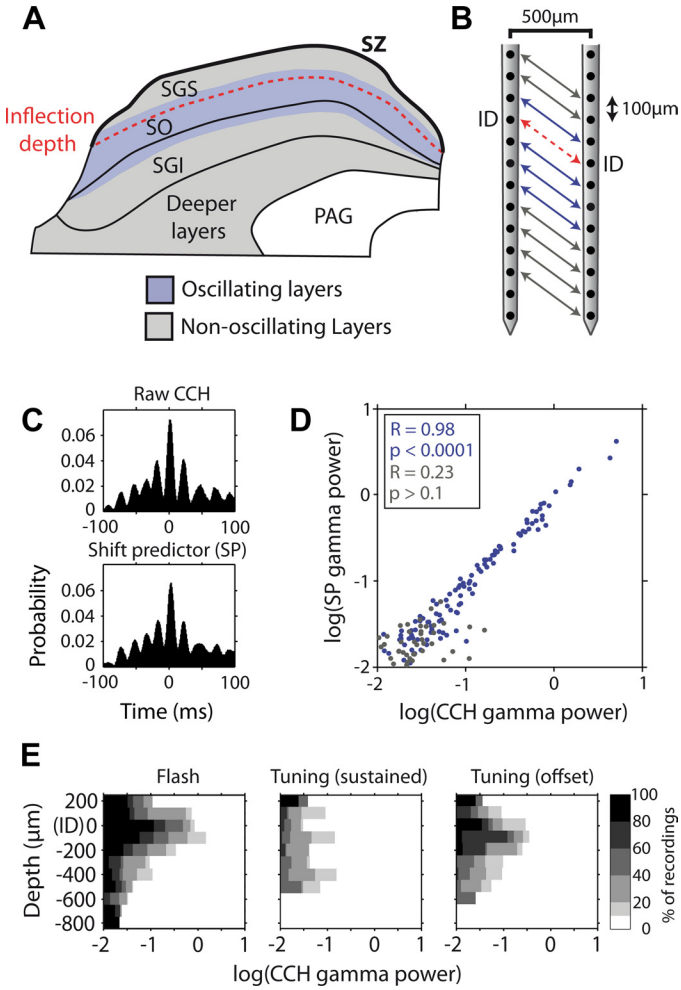

Fig. 9. Flash-evoked intershank spike correlation. *A*: diagram outlining the occurrence of evoked oscillatory activity across SC layers. The dotted red line indicates the anatomically inferred location of the ID. *B*: illustration how spike cross-correlation was computed between aligned contacts on both shanks. *C*: raw cross-correlation histograms (CCH) and shift predictor histograms calculated from two units displaying flash-evoked oscillatory activity at the same relative depth located on adjacent shanks. *D*: gamma power of CCHs plotted against the gamma power of shift predictor histograms for flash stimuli. Blue points represent contacts located close to the ID, with all other contacts plotted in gray. Correlation coefficients for each group are given with confidence scores. *E*: percentage of recording sites at each depth that displayed log(CCH gamma power) values between −2 and 1. Abbreviations: SZ, stratum zonale; PAG, periaqueductal gray.

discrepancy of gamma power between CCHs computed with shifted trials and aligned trials. Therefore, coherent oscillatory spiking activity observed horizontally within these layers is highly entrained to the flash stimulus, displaying little variability between consecutive trials. We repeated this analysis for the sustained and offset periods of drifting grating stimuli, with correlation coefficients and *P* values summarized in Table 3. Similar to flash-evoked responses, neurons located close to the ID displayed a highly significant correlation between CCH and SP gamma power following drifting grating stimulus offset ($R = 0.97$, $P < 0.0001$), with other layers displaying no correlation. The gamma power of CCHs computed between horizontally distributed neurons for flash and drifting grating stimuli are shown for all penetrations in Fig. 9*E*. CCH gamma power is shown for both sustained and offset periods of drifting grating stimulation. The strongest gamma oscillations were observed within the presumed SO layers following flash and grating stimulus offset. In contrast, there was no depth dependence of CCH gamma power throughout the sustained period of grating stimulation.

Table 2. *Correlation coefficient and P values for phase-locking values and oscillation score*

	R	*P*
Sustained*	0.17	>0.2
Sustained	0.63	<0.001
Offset*	0.6	<0.001
Offset	0.72	<0.001
Flash*	0.57	<0.001
Flash	−0.07	>0.5

*Upper stratum griseum intermediale, stratum opticum, and lower stratum griseum superficiale layers.

DISCUSSION

We report here a systematic study of the depth profile of visual response properties recorded simultaneously across the various layers of the ferret SC. Specifically, we investigated depth-activation profiles, response timing, spatial RF properties, and oscillatory activity by analyzing MUA and LFP responses to flash and drifting grating stimuli. In general, LFP and MUA responses displayed consistent depth profiles across all penetrations, most notably characterized by CSD depth profiles. In the SO and lower SGS regions, responses occurred with short latencies, with deeper layers responding with significantly longer latencies. The strongest visual responses were observed in superficial SC layers. Spatial RFs maintained topographic alignment across all visual responsive layers, with RFs centering on the same spatial location along each dorsoventral penetration. We observed the smallest MUA RFs in superficial layers, with deep layers displaying significantly larger RFs. In addition, some recording penetrations were characterized by strong stimulus locked gamma oscillatory activity in spikes and fields that was limited to the lower SGS, SO, and upper SGI layers. Stimulus-locked oscillations were evoked by flash stimulation and drifting grating stimulus offset and displayed strong spike-phase locking in the gamma frequency range. Gamma oscillations were also widely distributed laterally within layers, with spike correlations displaying strong temporal locking to the flash and grating stimulus offset.

Table 3. *Correlation coefficient and P values for cross-correlation histograms and shift predictor gamma power*

	R	*P*
Sustained*	0.36	<0.01
Sustained	0.03	>0.8
Offset*	0.97	<0.001
Offset	0.30	>0.1
Flash*	0.98	<0.001
Flash	0.23	>0.1

*Upper stratum griseum intermediale, stratum opticum, and lower stratum griseum superficiale layers.

Visual Responses Display Laminar Specificity

We found strong depth dependence for all measured visual response properties to flash stimulation. Perhaps most consistently, we observed a characteristic CSD depth profile, with current sources and sinks, or net inward and outward transmembrane currents, reflecting the approximate location of the anatomical border between the two main superficial SC layers, the SGS and SO. A previous report in awake rabbits reported the location of the ID more superficially in the upper SGS (Bereshpolova et al. 2006). However, the relative size of various SC layers, and the SGS in particular, is known to differ between species (Hilbig et al. 2000).

Reflecting the layer-specific termination of retinal afferents, we observed shortest latency responses in superficial layers, where fast projecting Y-type and slow projecting W-type retinal ganglion cells directly innervate the SO and SGS layers, respectively (Berson 1988a, 1988b; Berson and Stein 1995; Freeman and Singer 1983; Waleszczyk et al. 2004). In the cat, superficial collicular layers additionally receive direct inputs from early visuotopically organized cortical areas such as cytoarchitectonic areas 17, 18, 19, and to a lesser extent area 21a (Harting et al. 1992). In contrast to superficial collicular layers, in both cats (Berson 1988) and ferrets (Zhang and Hoffmann 1993), there is virtually no direct retinal input to the deep layers. Furthermore, unlike superficial layers, direct cortical inputs to deep collicular layers in both cats (Harting et al. 1992) and ferrets (Manger et al. 2010) originate from the "higher-order" visuotopically organized cortical areas. The range of latencies we observed across layers was consistent with previous work in the rat (Dommett et al. 2005; Thomas et al. 2004), cat (Altman and Malis 1962; Berman and Cynader 1975), and macaque monkey (Bell et al. 2006; Li and Basso 2008; Wurtz and Goldberg 1972). In addition to short-latency responses, we also consistently observed the most robust spiking responses in superficial layers, potentially reflecting a dominance of retinal inputs in the anesthetized preparation.

Despite SC layers receiving visual afferent inputs from distributed sources, previous tracing studies in the cat have shown that retinal and cortical terminals align along the dorsoventral axis of the SC, such that all layers form overlaid representations of contralateral visual space (Berson 1988a, 1988b; Feldon and Kruger 1970). Reflecting this organization of visual inputs, we observed strong alignment of spatial RFs along each shank. In addition, the relative shift of spatial RFs between probe shanks, with medial shank neurons responding to locations higher in the visual field, reflects the known topographical organization of the ferret SC (Quevedo et al. 1996). Although RFs were aligned along each shank, we observed strong depth dependence in RF size such that retinorecipient superficial layers displayed significantly smaller RFs than deeper layers. Previous studies in the cat (Brecht et al. 1999) and macaque monkey (Cynader and Berman 1972; Humphrey 1968) have also noted the tendency for RF size to increase with depth. However, this study represents the first systematic analysis of RF properties resolved with the laminar anatomy of the SC. Potentially accounting for the larger RFs observed in deeper layers is the relatively large radius of dendritic trees in SGI neurons (Isa and Hall 2009). Indeed, previous in vitro studies in rats (Helms et al. 2004; Isa et al. 1998) and tree shrews (Lee et al. 1997) have shown that stimulation of both directly overlying and off-axis superficial layer neurons to results in monosynaptic excitatory postsynaptic potentials in deeper SGI neurons. Therefore, the convergence of superficial-to-deep, or cortico-tectal projections on the large dendritic trees of deep layer neurons could account for the larger spatial visual RFs in these layers.

Stimulus-Locked Gamma Oscillatory Activity

We observed strong synchronous gamma oscillatory activity in spikes and field potentials limited to the lower SGS, SO, and upper SGI regions after flash stimulation and the offset of drifting gratings. Quantitative measures of oscillation strength, including oscillation score, PLV, CCH, and SP gamma power suggest that oscillations evoked by flash and grating stimuli offset are produced by similar mechanisms. In both the awake and anesthetized cat SC, Brecht and coworkers (1999, 2001) observed synchronous oscillations between distributed neurons in the alpha (8–12 Hz), beta (12–30 Hz), and gamma (40–60 Hz) frequency ranges, with the probability of synchronization depending on the congruency of visual stimuli and the overlap of RFs. Similarly, in the avian homologue to the mammalian SC, the optic tectum, gamma oscillations have also been implicated in coding spatial location of salient multimodal stimuli (Goddard et al. 2012; Neuenschwander et al. 1996; Sridharan et al. 2011). In contrast to previous studies, we observed very strong temporal locking of gamma oscillatory activity to visual stimuli. Therefore, the flash and grating-offset evoked gamma oscillations observed here are likely to reflect periodic entrainment of neurons in superficial SC layers by afferent inputs.

Possible Sources of Oscillatory Activity

Visually evoked gamma oscillations could originate from one (or a combination) of the following sources: retinal afferents, corticotectal inputs, or intrinsic network interactions. Since gamma oscillatory activity is spatially restricted to retinorecipient layers of the SC, retinal afferents may provide a source of coherent oscillatory inputs that entrain SC neurons under anesthesia. Indeed, Neuenschwander and coworkers (Neuenschwander and Singer 1996; Neuenschwander et al. 1999) reported high-frequency synchronous gamma oscillations coordinated between groups of retinal ganglion cells to light onset and light offset in the anesthetized cat. In response to stationary flash stimuli, lateral geniculate nucleus and cortical neurons reliably followed such retinal oscillations, indicating the feed-forward entrainment capacity of retinal and lateral geniculate nucleus efferents (Castelo-Branco et al. 1998).

An alternative source of coherent oscillatory inputs is the visual cortex. Indeed, previous studies have shown flash evoked oscillatory potentials in the visual cortex of anesthetized and awake cats and monkeys (Doty and Kimura 1963). In addition, synchronization of oscillatory activity between visual cortex and SC neurons has been previously reported in the anesthetized cat (Brecht et al. 1998). In the cat, early visual cortical areas 17 and 18 project to the superficial SC layers (Harting et al. 1992), suggesting that the same corticotectal inputs may provide a source of laminar-specific oscillatory entrainment in the ferret.

Computational models have shown that recurrent neuronal networks consisting of excitatory and inhibitory neurons produce reliable oscillations in the gamma frequency when $GABA_A$-mediated synapses produce feedback inhibition on excitatory neurons or other inhibitory interneurons (Buzsáki and Wang 2012). In an in vitro study of SO neurons in rat SC slices, Lo and coworkers (1998) showed that optic tract stimulation resulted in sharp excitation followed by smaller amplitude inhibition, suggesting these neurons receive feedback inhibition. In addition, SO neurons engaged in rhythmic gamma oscillations in response to membrane depolarizations and electrical optic tract stimulation. This study illustrates that the network mechanisms necessary for generating sustained horizontally distributed oscillatory activity are indeed intrinsic to the SC. Therefore, stimuli such as flashes and the offset of drifting gratings may represent sufficiently large transient inputs to trigger reverberations within horizontally distributed recurrent neuronal networks in the SC.

Effects of Isoflurane Anesthesia on Evoked SC Oscillations

In some experiments, oscillatory and nonoscillatory responses were recorded in close-by consecutive penetrations in the same animal, suggesting visually evoked oscillations are nonstationary. Imas and coworkers (2005) showed that the strength of flash-evoked gamma oscillations in the visual cortex of the rat was modulated in a concentration-dependent manner, with medium isoflurane levels producing strongest oscillatory power. While we tried to maintain the level of anesthesia constant throughout experiments, it is conceivable that nonstationarity in depth of anesthesia contributed to the variability with which flash-evoked gamma oscillations were observed. In addition, the depth of anesthesia most likely affects the interplay between bottom-up and top-down visual afferent inputs, with retinal afferents presumably being less affected by depth of anesthesia than cortical efferent pathways. Supporting this conclusion, Brecht and coworkers (2001) found that neurons in both superficial and deep SC layers in awake cats respond strongly to sustained natural and computer-generated visual stimuli. Taken together, these results suggest that anesthesia may exert little effects on bottom-up driven oscillations to transient stimuli, whereas induced oscillations, which typically display little temporal locking to the stimulus and may be cortically driven, are dampened in the anesthetized preparation.

Functional Implications of Entrained Gamma Oscillations

Since we recorded neural activity in the anesthetized ferret, we can only speculate on the role of entrained oscillations in the generation of motor behavior. However, a previous study using rhythmic electrical stimulation of the SC in awake cats does provide evidence that neuronal oscillations and synchrony may by informative for the generation saccadic eye movements (Brecht et al. 2004). In these experiments, synchronous electrical stimulation at distributed SC sites resulted in vector averaging of movement trajectories across stimulated areas, whereas asynchronous stimulation biased resultant movement trajectories toward vector summation. Coherent oscillations in superficial SC neurons may therefore unify responses to visual stimuli over SC areas, possibly acting to improve coincidence detection in downstream target neurons that control the rapid generation of motor commands (Salinas and Sejnowski 2000). However, further studies in awake behaving animals are required to clarify first the source of oscillatory entrainment, and second the influence oscillatory activity has on motor behavior.

ACKNOWLEDGMENT

We thank Dorrit Bystron for assistance throughout experiments and Doris Lange for performing histology.

GRANTS

This research was supported by funding from the Deutsche Forschungsgemeinschaft (GRK 1246/1-2; SFB 936/A2; A.K. Engel).

DISCLOSURES

No conflicts of interest, financial or otherwise, are declared by the author(s).

AUTHOR CONTRIBUTIONS

Author contributions: I.S. and A.K.E. conception and design of research; I.S., F.P., and G.E. performed experiments; I.S. analyzed data; I.S., E.G.-L., and A.K.E. interpreted results of experiments; I.S. prepared figures; I.S. drafted manuscript; I.S., E.G.-L., F.P., G.E., and A.K.E. edited and revised manuscript; I.S., E.G.-L., F.P., G.E., and A.K.E. approved final version of manuscript.

REFERENCES

Altman J, Malis Li. An electrophysiological study of the superior colliculus and visual cortex. *Exp Neurol* 5: 233–249, 1962.

Bell AH, Meredith MA, Van Opstal AJ, Munoz DP. Stimulus intensity modifies saccadic reaction time and visual response latency in the superior colliculus. *Exp Brain Res* 174: 53–59, 2006.

Bereshpolova Y, Stoelzel CR, Gusev AG, Bezdudnaya T, Swadlow HA. The impact of a corticotectal impulse on the awake superior colliculus. *J Neurosci* 26: 2250–2259, 2006.

Berman N, Cynader M. Receptive fields in cat superior colliculus after visual cortex lesions. *J Physiol* 245: 261–270, 1975.

Berson DM, Stein JJ. Retinotopic organization of the superior colliculus in relation to the retinal distribution of afferent ganglion cells. *Vis Neurosci* 12: 671–686, 1995.

Berson DM. Retinal and cortical inputs to cat superior colliculus: composition, convergence and laminar specificity. *Prog Brain Res* 75: 17–26, 1988a.

Berson DM. Convergence of retinal W-cell and corticotectal input to cells of the cat superior colliculus. *J Neurophysiol* 60: 1861–1873, 1988b.

Brainard DH. The Psychophysics Toolbox. *Spat Vis* 10: 433–436, 1997.

Brecht M, Goebel R, Singer W, Engel AK. Synchronization of visual responses in the superior colliculus of awake cats. *Neuroreport* 12: 43–47, 2001.

Brecht M, Singer W, Engel AK. Correlation analysis of corticotectal interactions in the cat visual system. *J Neurophysiol* 79: 2394–2407, 1998.

Brecht M, Singer W, Engel AK. Patterns of synchronization in the superior colliculus of anesthetized cats. *J Neurosci* 19: 3567–3579, 1999.

Brecht M, Singer W, Engel AK. Amplitude and direction of saccadic eye movements depend on the synchronicity of collicular population activity. *J Neurophysiol* 92: 424–432, 2004.

Buzsáki G, Wang XJ. Mechanisms of gamma oscillations. *Annu Rev Neurosci* 35: 203–225, 2012.

Castelo-Branco M, Neuenschwander S, Singer W. Synchronization of visual responses between the cortex, lateral geniculate nucleus, and retina in the anesthetized cat. *J Neurosci* 18: 6395–6410, 1998.

Cynader M, Berman N. Receptive-field organization of monkey superior colliculus. *J Neurophysiol* 35: 187–201, 1972.

Dommett E, Coizet V, Blaha CD, Martindale J, Lefebvre V, Walton N, Mayhew JEW, Overton PG, Redgrave P. How visual stimuli activate dopaminergic neurons at short latency. *Science* 307: 1476–1479, 2005.

Doty RW, Kimura DS. Oscillatory potentials in the visual system of cats and monkeys. *J Physiol* 168: 205–218, 1963.

Feldon P, Kruger L. Topography of the retinal projection upon the superior colliculus of the cat. *Vision Res* 10: 135–143, 1970.

Freeman B, Singer W. Direct and indirect visual inputs to superficial layers of cat superior colliculus: a current source-density analysis of electrically evoked potentials. *J Neurophysiol* 49: 1075–1091, 1983.

Goddard CA, Sridharan D, Huguenard JR, Knudsen EI. Gamma oscillations are generated locally in an attention-related midbrain network. *Neuron* 73: 567–580, 2012.

Grantyn R, Ludwig R, Eberhardt W. Neurons of the superficial tectal gray. An intracellular HRP-study on the kitten superior colliculus in vitro. *Exp Brain Res* 55: 172–176, 1984.

Hall WC, Lee P. Interlaminar connections of the superior colliculus in the tree shrew. I. The superficial gray layer. *J Comp Neurol* 332: 213–223, 1993.

Hall WC, Lee P. Interlaminar connections of the superior colliculus in the tree shrew. III. The optic layer. *Vis Neurosci* 14: 647–661, 1997.

Harting JK, Updyke BV, Van Lieshout DP. Corticotectal projections in the cat: anterograde transport studies of twenty-five cortical areas. *J Comp Neurol* 324: 379–414, 1992.

Hilbig H, Merbach M, Krause J, Gärtner U, Stubbe A. Dendritic organization of neurons of the superior colliculus in animals with different visual capability. *Brain Res Bull* 51: 255–265, 2000.

Humphrey NK. Responses to visual stimuli of units in the superior colliculus of rats and monkeys. *Exp Neurol* 20: 312–340, 1968.

Imas OA, Ropella KM, Ward BD, Wood JD, Hudetz AG. Volatile anesthetics enhance flash-induced gamma oscillations in rat visual cortex. *Anesthesiology* 102: 937–947, 2005.

Isa T, Endo T, Saito Y. The visuo-motor pathway in the local circuit of the rat superior colliculus. *J Neurosci* 18: 8496–8504, 1998.

Isa T, Hall WC. Exploring the superior colliculus in vitro. *J Neurophysiol* 102: 2581–2593, 2009.

Lachaux JP, Rodriguez E, Martinerie J, Varela FJ. Measuring phase synchrony in brain signals. *Hum Brain Mapp* 8: 194–208, 1999.

Li X, Basso MA. Preparing to move increases the sensitivity of superior colliculus neurons. *J Neurosci* 28: 4561–4577, 2008.

Lo FS, Cork RJ, Mize RR. Physiological properties of neurons in the optic layer of the rat's superior colliculus. *J Neurophysiol* 80: 331–343, 1998.

Manger PR, Restrepo CE, Innocenti GM. The superior colliculus of the ferret: cortical afferents and efferent connections to dorsal thalamus. *Brain Res* 1353: 74–85, 2010.

May PJ. The mammalian superior colliculus: laminar structure and connections. *Prog Brain Res* 151: 321–378, 2006.

Mureşan RC, Jurjuţ OF, Moca VV, Singer W, Nikolić D. The oscillation score: an efficient method for estimating oscillation strength in neuronal activity. *J Neurophysiol* 99: 1333–1353, 2008.

Neuenschwander S, Castelo-Branco M, Singer W. Synchronous oscillations in the cat retina. *Vision Res* 39: 2485–2497, 1999.

Neuenschwander S, Engel AK, König P, Singer W, Varela FJ. Synchronization of neuronal responses in the optic tectum of awake pigeons. *Vis Neurosci* 13: 575–584, 1996.

Neuenschwander S, Singer W. Long-range synchronization of oscillatory light responses in the cat retina and lateral geniculate nucleus. *Nature* 379: 728–732, 1996.

Nicholson C, Freeman JA. Theory of current source-density analysis and determination of conductivity tensor for anuran cerebellum. *J Neurophysiol* 38: 356–368, 1975.

Oostenveld R, Fries P, Maris E, Schoffelen JM. FieldTrip: Open source software for advanced analysis of MEG, EEG, and invasive electrophysiological data. *Comput Intell Neurosci* 2011: 156869, 2011.

Pistorio AL, Hendry SH, Wang X. A modified technique for high-resolution staining of myelin. *J Neurosci Methods* 153: 135–146, 2006.

Quevedo C, Hoffmann KP, Husemann R, Distler C. Overrepresentation of the central visual field in the superior colliculus of the pigmented and albino ferret. *Vis Neurosci* 13: 627–638, 1996.

Quiroga RQ, Nadasdy Z, Ben-Shaul Y. Unsupervised spike detection and sorting with wavelets and superparamagnetic clustering. *Neural Comput* 16: 1661–1687, 2004.

Salinas E, Sejnowski TJ. Impact of correlated synaptic input on output firing rate and variability in simple neuronal models. *J Neurosci* 20: 6193–6209, 2000.

Sridharan D, Boahen K, Knudsen EI. Space coding by gamma oscillations in the barn owl optic tectum. *J Neurophysiol* 105: 2005–2017, 2011.

Stein B, Meredith A. *The Merging of the Senses*. Cambridge, MA: MIT Press, 1993.

Stein BE, Wallace MT, Stanford TR. Development of multisensory integration: transforming sensory input into motor output. *Ment Retard Dev Disabil Res Rev* 5: 72–85, 1999.

Thomas BB, Seiler MJ, Sadda SR, Aramant RB. Superior colliculus responses to light-preserved by transplantation in a slow degeneration rat model. *Exp Eye Res* 79: 29–39, 2004.

Waleszczyk WJ, Wang C, Benedek G, Burke W, Dreher B. Motion sensitivity in cat's superior colliculus: contribution of different visual processing channels to response properties of collicular neurons. *Acta Neurobiol Exp (Warsz)* 64: 209–228, 2004.

Wurtz RH, Goldberg ME. Activity of superior colliculus in behaving monkey. 3. Cells discharging before eye movements. *J Neurophysiol* 35: 575–586, 1972.

Zhang HY, Hoffmann KP. Retinal projections to the pretectum, accessory optic system and superior colliculus in pigmented and albino ferrets. *Eur J Neurosci* 5: 486–500, 1993.